Distributed acoustic sensing as a tool for exploration and monitoring: a proof-of-concept

Nicola Piana Agostinetti[1,2], Alberto Villa[1], and Gilberto Saccorotti[3]

[1]DISAT, Universitá di Milano Bicocca, Piazza della Scienza 4, 20126, Milano, Italy
[2]Department of Geology, University of Vienna, Vienna, Austria
[3]Istituto Nazionale di Geofisica e Vulcanologia. Via Cesare Battisti 53, 56125 Pisa, Italy

Correspondence: Nicola Piana Agostinetti (nicola.pianaagostinetti@unimib.it)

Abstract. We use PoroTOMO experimental data to compare the performance of Distributed Acoustic Sensing (DAS) and geophone data in executing standard exploration and monitoring activities. The PoroTOMO experiment consists of two "seismic systems": (a) a 8.6 km long optical fibre cable deployed across the Brady geothermal field and covering an area of 1.5 x 0.5 km with 100m long segments, and (b) an array of 238 co-located geophones with an average spacing of 60m. The PoroTOMO experiment recorded continuous seismic data between March 10th and March 25th 2016. During such period, a M_L 4.3 regional event occurred in the southwest, about 150 km away from the geothermal field, together with several microseismic local events related to the geothermal activity. The seismic waves generated from such seismic events have been used as input data in this study. For the exploration tasks, we compare the propagation of the M_L 4.3 event across the geothermal field in both seismic systems in term of relative time-delay, for a number of configurations and segments. Defined the propagation, we analyse and compare the amplitude and the signal-to-noise ratio (SNR) of the P-wave in the two systems at high resolution. For testing the potential in monitoring local seismicity, we first perform an analysis of the geophone data for locating a microseismic event, based on *expert opinion*. Then, we a adopt different workflow for the automatic location of the same microseismic event using DAS data. For testing the potential in monitoring distant event, data from the regional earthquake are used for retrieving both the propagation direction and apparent velocity of the wavefield, using a standard plane-wave-fitting approach.

Our results indicate that: (1) at a local scale, the seismic P-waves propagation and their characteristics (i.e. SNR and amplitude) along a single cable segment are robustly consistent with recordings from co-located geophones (delay-times $\delta t \sim 0.3$ over 400 m for both seismic systems) ; (2) the interpretation of seismic wave propagation across multiple separated segments is less clear, due to the heavy contamination of scattering sources and local velocity heterogeneities; nonetheless, results from the plane-wave fitting still indicate the possibility for a consistent detection and location of the event; (3) at high-resolution (10m), large amplitude variations along the fibre cable seem to robustly correlate with near surface geology; (4) automatic monitoring of microseismicity can be performed with DAS recordings with results comparable to manual analysis of geophone recordings (i.e. maximum horizontal error on event location around 70 m for both geophones and DAS data) ; and (5) DAS data preconditioning (e.g., temporal sub-sampling and channel-stacking) and dedicated processing techniques are strictly necessary for making any real-time monitoring procedure feasible and trustable.

1 Introduction

Distributed acoustic sensing (DAS) is a novel technology that records ground vibrations, necessary for seismological investigations of the shallow crust (You, 2010; Jousset et al., 2018). DAS technology can be used to record vibrations of a optical fibre cable in terms of the derivative of the strain along the cable direction (Wang et al., 2018). DAS recordings of ground motion along a fibre cable can be obtained at unprecedented high-resolution (less than one meter, if necessary) without the need of deploying tons of instruments on the ground (Henninges et al., 2021). Moreover, DAS recordings can be obtained for Earth's regions which could be unfeasible to reach with standard seismological instruments (e.g. ocean floor, Lindsey et al., 2019). High-resolution seismic recordings are necessary for both the characterisation of next-gen geo-resources (e.g. Enhanced Geothermal System, EGS, or reservoirs for CO_2 storage), and the monitoring of geo-resources exploitation (e.g. monitoring of induced seismicity in geothermal wells, Li and Zhan, 2018).

The potential of DAS recordings to be used as "standard" seismic signals has been investigated in previous works (e.g. Yu et al., 2019). In general, DAS recordings can be used for locating off-shore seismic events (Marra et al., 2018) and reconstructing geological structures in the shallow crust (e.g. Ajo-Franklin et al., 2019). However, some concerns have been raised. For example, van den Ende and Ampuero (2020) highlights the difficulties in using DAS recordings with beam-forming techniques for locating events at large epicentral ranges (i.e., using the fibre as a standard seismic array). Moreover, partial coupling of the cable to the ground, especially for dark fiber, could be a challenge in harsh evironments (e.g. Sladen et al., 2019).

The PoroTOMO experiment investigated the Brady geothermal field with both conventional seismic instruments (238 short period 3-components seismometers) and 8.6 km of optical fibre cable (Feigl and The PoroTomo Team, 2017, see also: http://geoscience.wisc.edu/geoscience/people/faculty/feigl/porotomo/). PoroTOMO seismic data and DAS recordings have been previously analysed in numerous other studies (Zeng et al., 2017; Parker et al., 2018; Wang et al., 2018; Jreij et al., 2021) In particular, Wang et al. (2018) strictly compares the signal recorded from DAS channels and co-located seismometers for a M_L 4.3 regional event occurred near Hawthorne (about 150 km South-South-East from the test-site). The authors tested different theoretical approaches, like matching the difference of two geophone waveforms with the amplitudes of the sum of the DAS channels in-between, obtaining promising results. From application of template matching to DAS recordings, Li and Zhan (2018) detected microseismic activity at SNR below 1, which was then compared to the pumping history of the geothermal field (Cardiff et al., 2018).

In this study, we move a step-forward and test the potential of DAS recordings in terms of "exploration" of the underground and "monitoring" of seismicity. For "exploration", we mean the definition of spatial variations of elastic properties in the subsurface at high-resolution. With "monitoring", we have in mind those activities adopted for the real-time detection of "events" (in this case, seismic events). We build on the previous studies and we assume that DAS recordings are coherent to standard seismographic recordings, in the sense that the fibre cable is able to sense elastic waves traversing the rocks where the cable is deployed. From this starting point, we investigate: (1) how standard observables used in seismic exploration (and their spatial variation across the geothermal field) can be extracted from DAS recordings; and (2) how DAS recordings perform in the automatic detection and location of earthquakes at two different scales of epicentral distance, local and regional. In both cases,

we strictly compare the results obtained using DAS recordings, with similar analysis performed on co-located seismometers.
We anticipate here that the main differences of the results obtained with DAS recordings, with respect to standard seismology, are: (1) the necessity for treating a huge amount of data; and (2) the availability of horizontal recordings only, which impedes the use of standard analysis tools.

1.1 Geological background and the PoroTOMO experiment

The Brady geothermal system is located in the Hot Springs Mountains, northwestern Nevada, USA. The geothermal reservoir lies within layered Tertiary volcanic rocks covered by a sedimentary layer of variable thickness (Jolie et al., 2015). The bottom of the geothermal reservoir is constituted by a Mesozoic metamorphic and plutonic crystalline basement, which is found at depths between 600 and 1500 m below the surface.

The main structural feature of the area is the Brady's fault zone, a fault system extending for some 10km with a dominant NNE strike and steeply dipping to the NW. The geothermal system is strictly related to the presence of those steeply dipping normal faults, where dilatation at depth promotes the fluids circulation (Faulds et al., 2006). The Brady geothermal system is the only one in the area that displays surface geothermal phenomena, for about 4–km along the Brady fault zone. In the area of interest, such geothermal phenomena (e.g. fumaroles warm-grounds and mud-volcanoes) are found, mainly distributed in-between the surface expression of two branches of the Brady fault (Figure 1). The Brady geothermal field is classified as *high entalpy* geothermal resource, reaching a temperature close to $180°$ (Shevenell and De Rocher, 2005).

PoroTOMO experiment (Feigl and Parker, 2019) covers the Northwestern part of the Brady geothermal field where subsidence have been observed in the past (Ali et al., 2016). In the PoroTOMO area, close to the locations of several injection wells, water circulation models suggest that almost horizontal water flow at shallow depth should occur from the North-West toward the southern portion of the geothermal field. The PoroTOMO experiment tested different technologies and different tools for the analysis of the ground deformation of the Brady geothermal field, during a predefined sequence of human activities at the geothermal wells (e.g. repeated injections). All geophysical data recorded and collected during PoroTOMO experiment can be found on GDR repository (Feigl and POROTOMO team, 2016), together with information on the geothermal operations. Among the others, data from the PoroTOMO experiment has been used for: comparison of catalogs of microseismicity and pumping records on a daily basis (Cardiff et al., 2018), detection of microseismic events through template matching applied to DAS data (Li and Zhan, 2018), active seismic tomography (Parker et al., 2018), comparison of DAS and geophone data for regional seismic waves (Wang et al., 2018) and evaluation of beamforming potential in DAS data (van den Ende and Ampuero, 2020).

2 Data and Methods

We make use of DAS recordings acquired during March 2016 in the framework of the PoroTOMO experiment (Feigl and The PoroTomo Team, 2017). The optical fibre cable was deployed with a zig-zag geometry composed of 71 contiguous seg-

90   ments; on average, the length of individual segments was on the order of 150 m. Relevant segments used in the next sections
are numbered in Figure 1. Acquisition gauge length is fixed to 10 m, with channel sampling every 1 m, (Wang et al., 2018).

For the exploration tasks, described in section 3.1, we use one channel every gauge length (10 m) and discard the channels
too close (10 m) to the bending point of the cable (as done in Wang et al., 2018). Given the segment length and the gauge length,
we obtain about 10-15 independent acoustic records for each segment. The acoustic signal are recorded at 1000 sps. DAS data

95   are organised in 30-seconds long HDF5 files, about one 1Gb for each file. In parallel, we also downloaded and analysed data
recorded by a co-located array of 238 Nodal geophones (Fairfield Nodal ZLand 3-component short period seismometers, with
a peak frequency of 4.5Hz, called "nodes" hereinfater). Nodes had been deployed as close as possible to the fibre, allowing a
detailed comparison of the signal recorded by the DAS and nodes systems.

We make use of the waveforms relative to the M_L 4.3 Hawthorne event. For the exploration tasks, the analysis is limited to

100   P-wave arrival. P-wave can be clearly seen in both DAS ad Nodes recording (Figure 2). Here, we filter the waveforms between
0.5 and 2 Hz, enhancing the earthquake signal. DAS recordings are downsampled to 500 sps, to be consistent with nodes
recordings. To compare nodes to DAS recordings, horizontal components of the nodes are rotated to match the azimuth of the
closest segment of fibre cable (Figure 1). All computations on nodal recording are operated on the rotated seismograms, if not
specified.

105   The analysis of the M_L 4.3 event consists in the automatic determination of the relative P-wave arrival times for each
segment of fibre cable and for all co-located nodes. The P-wave time delays are computed following the approach described
in VanDecar and Crosson (1990) and in Piana Agostinetti and Martini (2019). For each of the three experiments (see Section
3.1), we compute the P-wave time delays for the selected DAS channels (one every 10 m). Following VanDecar and Crosson
(1990), we first compute (1) the time-delay between all couples of selected channels, cross-correlating a 2 s long time window;

110   and then (2) the absolute time-delay δt_i for the i-th selected channel under the condition of $\sum_i \delta t_i = 0$. The same procedure is
performed for the oriented horizontal recordings of the co-located nodes. After the definition of the time-delays, we measure
the SNR for each channel and each node, considering a 5 s long time-window before and after the P-wave arrival (Figure 2).
On the same time-window that contains the P-wave, we also measure the maximum amplitude.

For monitoring tasks, we consider two test cases of earthquakes recorded at regional and very local ranges. For the former

115   case, we use the aforementioned Hawthorne earthquake. For the latter one, we review the catalogue of microseismicity found
in Li and Zhan (2018) spanning the entire Brady geothermal field, and select one event that occurred on 2016 March 14 -
10:41:576UTC, in close proximity of the node and DAS deployments.

The local earthquake as recorded by the nodes is processed to obtain a reference location. Precise P- and S-wave arrival
times are derived from manual picking at 75 vertical and 48 horizontal channels. Theoretical travel times are calculated in a

120   homogeneous half-space, with compressional (V_P) wave velocity of 3 km/s (Zeng et al., 2017; Parker et al., 2018) and a ratio
between Vp and S-wave velocity (V_S) $V_P/V_S = 2.8$, as indicated by the modified Wadati diagram. The likelihood function for
source location has been explored using the Octet-tree sampling method (Lomax et al., 2009). Analysis of the same event at the
DAS deployment begins by band-pass filtering over the 15-40Hz frequency band, followed by subsampling at 100Hz. A spatial
sub-sampling is then performed by stacking the recordings from 11 adjacent channels within each profile, with a 20-channel

125 step. The 20 channels before and after each corner point are excluded. This procedure results in a virtual array composed by 274 channels, thus similar to the nodal array. For each stacked trace, we then calculate a characteristic function given by the Kurtosis (Langet et al., 2014), and use an AIC autopicker (Sleeman and van Eck, 1999) to automatically identify the onset time of these functions. Finally, we use the DBSCAN algorithm (Ester et al., 1996) to discard the most obvious outliers, thus obtaining a set of 243 estimates of arrival times. Using the same simplified velocity structure described above, these data are

130 finally inverted for a source location using both a conventional travel-time inversion as for the nodal array data, and a likelihood function based on the Equal Differential Time [EDT] formulation (Font et al., 2004; Lomax, 2005). In this latter method, the likelihood of a given model is expressed as the sum of a set of probability density functions which, for any independent channel pair, incorporate the squared difference between the observed and predicted differential times at that pair. The EDT likelihood function is thus particularly appealing given its robustness in the presence of outliers, i.e. observations whose residuals are

135 greater than the nominal uncertainty (Lomax, 2005).

For the Hawthorne earthquake, 2-minute-long DAS recordings are first band-pass filtered over the 0.5-2Hz frequency band, and then sub-sampled at 100Hz. Spatial sub-sampling is performed in a similar manner to what described above, but stacking over 41 adjacent channels with a 40-channel step, thus obtaining a virtual array of 57 elements. Delay times $\Delta T_{ij}, i \neq j$ between all the independent array channels are derived from the maxima CC^{max} of the corresponding cross-correlation function;

140 these differential times are used to derive the horizontal slowness vector according to the linear relationship (Del Pezzo and Giudicepietro, 2002):

$$\Delta \boldsymbol{T} = \Delta \boldsymbol{x} \cdot \boldsymbol{s} \tag{1}$$

where the matrix $\Delta \mathbf{x}$ contains the differences between the x (EW) and y (NS) components of the array channel's coordinates, and $\boldsymbol{s}$ is the horizontal slowness vector, from which we derive the propagation azimuth (measured clockwise from the N

145 direction) and apparent velocity.

Equation 1 is solved using a weighted least-squares approach, with weights defined as:

$$w_{ij} = \frac{CC_{ij}^{max}}{1 - CC_{i1}^{max}} \tag{2}$$

so to emphasize the contribution of the most correlated channels. For the inversion, we considered only those channel pairs exhibiting a CC^{max} larger than an arbitrary threshold, here set equal to 0.85. The procedure is iterated over 4-s-long time

150 windows, sliding along the DAS recordings with 80% overlap.

3 Results

3.1 Exploration

Direct comparison of DAS and Nodal recordings is not possible, due to the sensitivity of the two seismic systems to different geo-observables. Many different procedures have been developed to convert DAS recordings to Nodal recordings and viceversa

155 (Wang et al., 2018, and references therein). Here we do not aim to use the two systems together in the same analysis, but to

compare the performance of the two systems on the same analysis workflow. Thus we do not transform one system into the other, but we use them separately. However, for only one case, we start our analysis reproducing the results obtained in Wang et al. (2018) for comparing the two systems using the amplitudes of the sum of several DAS strain-rate waveforms along a segment and the finite difference of two geophone waveforms at the two ends of the same segment. We use the DAS data

160 recorded along segment 15, where 4 nodes have been co-deployed (Figure 3). This allows us to divide the segment 15 into three sub-segments and analyse each sub-segment as an independent set of information (i.e. only data from the four geophones have been used twice). We make use of the workflow of Wang et al. (2018, Figure 9 and equation 5), composing a "representative DAS waveform" from the sum of one channel of DAS data every 10 m in between two geophones and comparing it to the "finite-difference Nodal waveform" of the two geophone waveforms. Our results confirm the finding in Wang et al. (2018),

165 where the authors indicate that the amplitude recorded by the two systems are coherently correlated. We also observe, as found in Wang et al. (2018), a small absolute time-delay between the two systems, that we correct cross-correlating the "representative DAS waveform" with the finite-difference Nodal waveform.

The propagation of the P-wave generated by the M_L 4.3 event can be easily tracked across the PoroTOMO investigated area using the vertical components of the geophones. Such analysis can be used as a reference of the general propagation direction

170 and time-delay. To get a first insight on the potential local anomalies in the P-wave propagation, we process vertical and North components of the nodes. In this case, we make use of the same tool (i.e. cross-correlation of the waveforms following VanDecar and Crosson, 1990) without rotating the horizontal as described in the previous section. Vertical components of the nodes clearly display similar P-wave arrivals, and the cross-correlation procedure gives correlation coefficients as high as 0.96-0.99 on average (Figure 4). Mapping the time-delay obtained through with the application of VanDecar and Crosson (1990) s

175 approach shows a South-South-East to North-North-West propagation as expected (Figure 5a). On the contrary, repeating the same analysis for the North component of the nodes and mapping the results, we observe that the wave propagation is more complex showing, for example, an area in the center of the nodal array, where strong negative time-delay are observed (Figure 5b). Those could be apparent anomalies given by local surface waves generated from interaction of the P-wave with the local topography and erroneously cross-correlated with the correct P-wave. Nevertheless, this result supports our workflow where

180 DAS data need to be strictly compared to co-located, re-oriented Nodal data.

We present a first analysis on the P-wave recorded by the DAS system, considering DAS segment 48. This segment is the longest one (about 350 m), with 7 geophones almost co-located along the cable (within 30m), and it gives us the possibility of following the P-wave over a long distance (Figure 7). P-waves recorded along the cable are generally similar, but not as much as on the vertical components of the Nodal system, giving smaller cross-correlation coefficients (about 0.95 on the average,

185 Figure 6), with some waveforms displaying large pre-signal noise (channel 5534 and 5524 in Figure 6a). Mapping the time-delays and the other quantities for the two systems shows that the time-delays are generally consistent, decreasing from 0.19 s to -0.05 s (with a minimum of -0.10 s) for the nodes and from 0.19 s to -0.15 s for the DAS data. Maximum amplitude in the two systems also displays similar spatial trends. More interesting, SNR in the DAS system has a sudden drop at about X=-100 m in our profile projection (Figure 7d), where we also observe the nosiest waveforms (Figure 6a), possibly indicating a partial

190 failure in the cable coupling to the ground. However, such defect (if existent) does not bias the time-delay measurement.

We repeat the same experimental setting for three, near parallel and consecutive, DAS segments: 28, 33, 68. Those segments
have an average azimuth of N30W, but are not contiguous, and almost cover a 500 m long profile. Nine geophones have
been deployed close to such segments (Figure 8). Also in this case, the spatial variations of time-delay, SNR and maximum
amplitude between the two systems is coherent. SNR does not vary significantly, with a small decrease toward South. Maximum
195 amplitude displays a sharp decrease from North to South in both system, in the very first hundred meters. The two systems
are not perfectly coherent, but one geophone out of three is far from the cable (about 50 m). Time-delay shows contrasting
evidence in the two system at the end of the profile toward South. While the overall trends in the two system is coherent (i.e.
largest value sin the central portion of the profile and smallest at the two ends), a 60 m long cable section of segment 68 show
time-delays as small as -0.20 s, not found in the geophone data. A close inspection to the waveforms (Figure 8ef) reveals the
200 presence of possibly scattered waves in DAS recordings at channel 8179 (i.e. strong differences from channel 8199, not found
in the Nodal system, where differences in the recordings of co-located nodes, N046 and N069, are minimal).

To test the possibility of appreciating 3D features, we apply our workflow to two parallel segments, 3 and 5 that run along
the longer side of a rectangular area of about 150 x 70 m. Eight geophones are deployed along the two segments (4 geo-
phones/segments, Figure 9). The results indicate that both time-delays and maximum amplitude display the same spatial vari-
205 ation. In particular, time-delay ranges between -0.12 s and 0.12 s for both systems and indicate an un-expected East-to-West
propagation. Amplitude variation are coherent in both system, increasing toward West. In this case, we notice that channels
close to the end of the segments are generally different from the closest one. We suggest that the practise of removing the
channels closer to the bending point of the fibre should be revised increasing the lag distance, now 10 m (a lag of 15 m or 20
m could work finely).

210 Finally, we analysed separately all segments between 1 and 30, covering the Northwestern side of the PoroTOMO ex-
periement, where most of the geothermal phenomena are found bounded by two faults mapped at the surface (i.e. fumaroles
and warm-ground, Figure 10). The variations of the maximum amplitude show that the highest values are found in the only
two places where the fibre cable crosses the geothermal active area (i.e. near the northernmost fumaroles and where warm
ground is mapped) roughly traversing the two bounding faults. Given the nature of the geothermal phenomena, we suggest
215 that amplitude variations in this case could be related to local site effects associated with the development of the underground
fracture network.

3.2 Monitoring

3.2.1 Local Earthquake

Figure 11 illustrates the comparison between the reference location obtained from manual picking of nodal data, and those de-
220 rived from the automatic processing of the DAS virtual array. Location from the nodal deployment indicate a well-constrained
source volume located at the center of the SW margin of the deployment, at a depth of $450[\pm40]$m beneath the surface (Figure
11a). Horizontal uncertainties are on the order of 36m and 71m for the EW- and NS-component, respectively; the root-mean-
square of residuals (RMS) is 0.05s. When applied to the automatic DAS pickings, the same standard location procedure did

7

not converge to a solution, since the exploration of the likelihood function clipped at the southern boundary of the searching
grid (Figure 11b). Conversely, EDT performs excellently in inverting the same set of automatic observations, leading to an
epicentral estimates basically coincident with the reference one. Horizontal uncertainties of this location are on the order of
28m and 71m for the EW- and NS-component, respectively; RMS is 0.07s. However, the estimate of source depth (a few meters
below the surface) is not compatible with the reference one, even considering the associated uncertainty which is on the order
of 75m. This discrepancy likely owes to the lack of observations attributed to S-waves, and the simplified velocity structure
adopted for travel-time predictions.

The reason of the different topology exhibited by the ''conventional'' and EDT likelihood functions relies on the large scatter
of onset times automatically estimated at the DAS channels (Figure 11d). Such scatter, in addition to the propagation effects
highlighted in the previous section, is also a consequence of the fact that DAS only senses the projection onto the fiber of
the horizontal component of the P-wave particle motion. Many onsets, therefore, are likely representative of S-wave arrivals,
following either direct or scattered paths. The EDT approach, however, performs efficiently in down-weighting such arrivals,
selectively attributing larger importance to those observations which are most consistent with the predictions (Figure 11d).

3.2.2 The Hawthorne earthquake

In addition to what described in the previous Section, the DAS recordings from the Hawthorne earthquake have already been
analyzed in Wang et al. (2018) and van den Ende and Ampuero (2020). In particular, this latter study compared the perfor-
mance of the DAS and nodal arrays in seismic beamforming for deriving the propagation parameters (apparent velocity and
propagation azimuth) for the direct P- and S-wave arrivals. In their work, van den Ende and Ampuero (2020) applied the MU-
SIC method (Goldstein and Archuleta, 1987) to different combination of DAS channels; in no case, however, did they obtained
results compatible with what expected for a single plane wave propagating along the source-to-receiver direction. This occur-
rence was attributed to marked velocity heterogeneities and scattering sources, locally distorting the wavefront and producing
loss of signal coherence, in turn masking the weaker P-wave signal impinging at the array with steep incidence angles. Follow-
ing this observation, van den Ende and Ampuero (2020) concluded that '....*the DAS array exhibits poor waveform coherence
and consequently produces inadequate beamforming results that are dominated by the signatures of shallow scattered waves*'.

Although these conclusions are fully consistent with the complex wave propagation we outlined above, our application of
the PWF approach to the sub-sampled DAS recordings yields to promising results (Figure 12). As a matter of fact, the onset
of the earthquake signal is marked by an abrupt increase of the average multi channel correlation (Figure 12b) which, in
correspondence of the P-wave arrival, peaks to a value which is about 2 times larger than those associated with the preceding
background noise. The P-wave propagation azimuth associated with the most-correlated arrivals are biased by some $30°$ with
respect to what expected from the source location. The apparent velocities associated with the most-correlated portion of the
P-wave arrival are in within the 4-6 km/s range, consistent with the 5-6 km/s range estimated by van den Ende and Ampuero
(2020) using data from the nodal array. Similar consistency is observed for the S-wave arrival, even if its onset is less clear due
to contamination by the P-coda wavetrain.

Overall, the results from this exercise suggest that: (i) stacking of adjacent channels within individual profiles serves to alleviate losses of waveform coherence due to local medium heterogeneities, thus increasing the overall wavefield coherence

260   throughout the DAS deployment; (ii) a simple thresholding on the overall correlation of DAS channels may serve as an efficient operator for detecting the arrival of an earthquake signal, and (iii) although with some bias, the estimates of P-wave direction of propagation and apparent velocity are reliable enough to obtain a preliminary estimate about the location of the source.

4   Discussions

Our analysis confirms that DAS recordings can be used as complementary or in substitution of standard geophones for both

265   monitoring activities and exploration of the the subsurface. Taking into account the limitations of DAS recordings, several challenges should be addressed in the future for enabling the use of such data in, e.g., standard monitoring routines. Those challenges arise mainly from the intrinsically different structure of the data obtained from the fibre cable with respect to what is recorded from a set of single-vertical or 3C geophones, more than from the two different physical observables recorded by DAS and geophones. DAS data structure is characterised by a huge amount of observations of the seismic waves along (1) an

270   horizontal axis, and (2) with a relatively poor areal coverage with respect to a standard seismic network. Exploiting such data structure would probably require to re-think the "old style" approaches to seismic data analysis, which have been developed since the '70 mostly for areal distributions of individual vertical geophones.

Our analysis of the DAS and geophone data substantiates previous findings that horizontal and vertical recordings gives different images of the propagation of distant events across a seismic array. This is a fundamental point to be kept in mind

275   when analysing DAS data, which are, by definition, only horizontal (in most-used, standard configuration of the fibre cable). Local scattering of surface waves given by topographic roughness could negatively interfere with the propagation of the P-wave potentially suppressing first arrivals and biasing the measure of, e.g., relative time-delays.

Looking into the details of the propagation of the P-wave of a regional event along segments of fibre cable, we observe that local variations of standard measures (time-delays, SNR and maximum amplitude of the signal) are consistent between

280   fibre cable and co-located geophones. In particular, we found that the analysis of the data recorded by a single segment of fibre cable shows the most stable results, even in case of poor coupling of the fibre. Analysing the data for multiple, parallel, not-consecutive segments provides unclear results, likely as a consequence of scattering and wavefront distortion induced by local velocity heterogeneties. In a case, the two parallel not-aligned segments, results are definitely promising, with potential for 3D subsurface reconstructions. In the case of a profile composed of three separated segments, results are ambiguous and

285   need further investigations. Analysing each single segments on the North-West side of the PoroTOMO experiment where the geothermal phenomena are found (warm grounds and fumaroles), we are able to correlate, at a higher resolution with respect to geophones, amplitude variations of the recorded signal with local near surface geology.

Our monitoring test clearly demonstrates the need of a preliminary selection of the data before locating seismic events. In DAS data, seismic phase recognition can be more difficult than in geophone data, due to the absence of vertical recordings

290   which are most sensitive to the P-wave arrival. S-wave can be easily mis-picked as P-wave at more distant or less favourably-

oriented segments, where the background noise can mask the very first onset of longitudinal waves. DAS data analysis must thus relies on specific methodologies where the consistence of the data themselves with the underlying hypothesis is statistically evaluated and accounted for. The EDT approach adopted here gives promising results by effectively down-weighting those observations which are not consistent with the predictions; nonetheless, its actual effectiveness needs to be thoroughly verified on further test cases. Within this context, it is worth mentioning a statistical approach developed recently, which consistently defines, in a Bayesian sense, the "membership" of each datum to the "outliers" class, and which could help further developments of DAS data treatment (Tilmann et al., 2020).

Results from the plane-wave fitting processing of the regional earthquake suggest that reliable event detection and location may be achieved, providing some simple (i.e., channel-stacking) procedure is adopted. A natural question thus regards the differences between these latter results and those derived by van den Ende and Ampuero (2020).

First, we note that the initial beamforming estimates by van den Ende and Ampuero (2020) were obtained using the entirety of the DAS channels. This may have contributed to attributing larger weight to those intra-profile channels that, though being very coherent, were dominated by locally-scattered waves. On the contrary, our intra-profile channel-stacking procedure has likely served to alleviating the effects of medium heterogeneities at spatial scales smaller than, or comparable to, the length of individual profiles. Second, van den Ende and Ampuero (2020) applied the MUSIC method assuming a single plane-wave; under this circumstance, the (possibly many) secondary yet correlated sources are erroneously attributed to the noise subspace, thus introducing a bias by the time of minimizing the projection of the theoretical signal onto that space.

Within this context, we also note that the huge amount of available channels in DAS systems is perfectly suited for application of processing techniques that improve both accuracy and precision of existing frequency-wavenumber methods, such as sub-array spatial averaging (e.g. Goldstein and Archuleta, 1991).

Finally, we voluntarily skip an important task in seismic monitoring systems: the definition of the event magnitude. We are aware that such task would require additional work to be fulfilled with DAS data. Amplitude variations could be high in DAS recordings from close-by channels, limiting the potential of using such kind of data for magnitude estimations. However, in case of the availability of a large number of events, we can anticipate that, due to the amount of data retrieved from the fibre cable, state-of-the-art approach to data mining should be able to fulfill the task (e.g. supervised machine learning).

5   Conclusions

We make use of DAS recordings obtained during PoroTOMO experiment (Brady geothermal field), for testing their potential in simple exploration and monitoring tasks. We analyse waveforms from a regional events, to get insights into the local structure of the geothermal field, and from a local microseismic event, to perform precise automatic event location. Our main findings are:

1. DAS recordings can be used for monitoring and exploration purposes and their performance is at least comparable to seismological records if not superior. For the monitoring task, we showed the that simple pre-processing schemes, such

as channel-stacking, spatial subsampling and band-pass filtering, if tailored to the wavelength of interest permits an effective approach to both the detection and location problems.

325   2. DAS recordings can not be strictly treated as standard seismic recording due to the large amount of data. Data selection is definitely necessary and open additional questions on the use of DAS recording (i.e. who selects the data in an automatic system?);

3. DAS recordings represent horizontal ground-displacement only, which limits, in some sense, the use of standard seismo-logical analysis tools depicted specifically for the processing of vertical or 3D ground-motion. To this respect, if used as

330   a seismic antenna, DAS should be deployed according to multiple segments oriented along a large variety of azimuths, so to increase the overall sensitivity toward distinct wavetypes propagating along different directions;

4. Although potential and limitations of DAS systems as a seismic antenna need further investigation, the promising performances of DAS toward detection of signals at low SNR (e.g. Li and Zhan, 2018) suggests that multiple DASs in network configuration (Ward Neale et al., 2018) could represent the evolution of current deployments for earthquake monitoring

335   at the local and regional scales.

New monitoring and exploration tools developed for DAS recordings are needed. In particular, exploration of the DAS data-space (Tarantola, 2005) would give an important contribution toward the analysis of DAS recording in a semi-automatic system.

References

Ajo-Franklin, J. B., Doou, S., and et al., N. J. L.: Distributed Acoustic Sensing Using Dark Fiber for Near-Surface Characterization and Broadband Seismic Event Detection, Sci. Rep., 9, 1328, https://doi.org/10.1038/s41598-018-36675-8, 2019.

Ali, S., Akerley, J., Baluyut, E., Cardiff, M., Davatzes, N., Feigl, K., Foxall, W., Fratta, D., Mellors, R., Spielman, P., Wang, H., and Zemach, E.: Time-series analysis of surface deformation at Brady Hot Springs geothermal field (Nevada) using interferometric synthetic aperture radar, Geothermics, 61, 114–120, https://doi.org/https://doi.org/10.1016/j.geothermics.2016.01.008, 2016.

Cardiff, M., Lim, D. D., Patterson, J. R., Akerley, J., Spielman, P., Lopeman, J., Walsh, P., Singh, A., Foxall, W., Wang, H. F., Lord, N. E., Thurber, C. H., Fratta, D., Mellors, R. J., Davatzes, N. C., and Feigl, K. L.: Geothermal production and reduced seismicity: Correlation and proposed mechanism, Earth and Planetary Science Letters, 482, 470–477, https://doi.org/https://doi.org/10.1016/j.epsl.2017.11.037, 2018.

Del Pezzo, E. and Giudicepietro, F.: Plane Wave Fitting Method for a Plane, Small Aperture, Short Period Seismic Array: A MATHCAD Program, Comput. Geosci., 28, 59–64, https://doi.org/10.1016/S0098-3004(01)00076-0, 2002.

Ester, M., Kriegel, H.-P., Sander, J., Xu, X., et al.: A density-based algorithm for discovering clusters in large spatial databases with noise., in: Kdd, vol. 96, pp. 226–231, 1996.

Faulds, J. E., Coolbaugh, M., Vice, G. S., and Edwards., M. L.: Characterizing Structural Controls of Geothermal Fields in the Northwestern Great Basin- A Progress Repor, in: Transactions. GRC Annual Meeting, pp. 69–76, Geothermal Resources Council, 2006.

Feigl, K. and The PoroTomo Team: Overview and Preliminary Results from the PoroTomo project at Brady Hot Springs, Nevada: Poroelastic Tomography by Adjoint Inverse Modeling of Data from Seismology, Geodesy, and Hydrology, in: 42nd Workshop on Geothermal Reservoir Engineering, Stanford University, 2017.

Feigl, K. L. and Parker, L. M.: PoroTomo Final Technical Report: Poroelastic Tomography by Adjoint Inverse Modeling of Data from Seismology, Geodesy, and Hydrology, Tech. rep., Univ. of Wisconsin, Madison, WI (United States), 176 pp, 2019.

Feigl, K. L. and POROTOMO team: Retrieved from https://dx.doi.org/10.15121/1721671, 2016.

Font, Y., Kao, H., Lallemand, S., Liu, C.-S., and Chiao, L.-Y.: Hypocentre determination offshore of eastern Taiwan using the Maximum Intersection method, Geophysical Journal International, 158, 655–675, https://doi.org/10.1111/j.1365-246X.2004.02317.x, 2004.

Goldstein, P. and Archuleta, R. J.: Array analysis of seismic signals, Geophysical Research Letters, 14, 13–16, https://doi.org/https://doi.org/10.1029/GL014i001p00013, 1987.

Goldstein, P. and Archuleta, R. J.: Deterministic frequency-wavenumber methods and direct measurements of rupture propagation during earthquakes using a dense array: Theory and methods, Journal of Geophysical Research: Solid Earth, 96, 6173–6185, https://doi.org/https://doi.org/10.1029/90JB02123, 1991.

Henninges, J., Martuganova, E., Stiller, M., Norden, B., and Krawczyk, C. M.: Wireline distributed acoustic sensing allows 4.2 km deep vertical seismic profiling of the Rotliegend 150 °C geothermal reservoir in the North German Basin, Solid Earth, 12, 521–537, https://doi.org/10.5194/se-12-521-2021, 2021.

Jolie, E., Moeck, I., and Faulds, J. E.: Quantitative structural–geological exploration of fault-controlled geothermal systems—A case study from the Basin-and-Range Province, Nevada (USA), Geothermics, 54, 54–67, https://doi.org/https://doi.org/10.1016/j.geothermics.2014.10.003, 2015.

380   Jousset, P., Reinsch, T., Ryberg, T., Blanck, H., Clarke, A., Aghayev, R., Hersir, G. P., Henniges, J., Weber, M., and Krawczyk, C.: Dynamic strain determination using fibre-optic cables allows imaging of seismological and structural features, Nat. Comm, 9, 2509, https://doi.org/10.1038/s41467-018-04860-y, 2018.

Jreij, S. F., Trainor-Guitton, W., Morphew, M. D., and Ning, I. L. C.: The Value of Information From Horizontal Distributed Acoustic Sensing Compared to Multicomponent Geophones Via Machine Learning, Journal of Energy Resources Technology-transactions of The Asme,
385   143, https://doi.org/10.1115/1.4048051, 2021.

Langet, N., Maggi, A., Michelini, A., and Brenguier, F.: Continuous kurtosis-based migration for seismic event detection and location, with application to Piton de la Fournaise Volcano, La Reunion, Bulletin of the Seismological Society of America, 104, 229–246, 2014.

Li, Z. and Zhan, Z.: Pushing the limit of earthquake detection with distributed acoustic sensing and template matching: a case study at the Brady geothermal field, Geophysical Journal International, 215, 1583–1593, https://doi.org/10.1093/gji/ggy359, 2018.

390   Lindsey, N. J., Dawe, T. C., and Ajo-Franklin, J. B.: Illuminating seafloor faults and ocean dynamics with dark fiber distributed acoustic sensing, Science, 366, 1103–1107, https://doi.org/10.1126/science.aay5881, 2019.

Lomax, A.: A reanalysis of the hypocentral location and related observations for the great 1906 California earthquake, Bulletin of the Seismological Society of America, 95, 861–877, 2005.

Lomax, A., Michelini, A., and Curtis, A.: Earthquake Location, Direct, Global-Search Methods, pp. 2449–2473, Springer New York, New
395   York, NY, https://doi.org/10.1007/978-0-387-30440-3_150, 2009.

Marra, G., Clivati, C., Luckett, R., Tampellini, A., Kronjäger, J., Wright, L., Mura, A., Levi, F., Robinson, S., Xuereb, A., Baptie, B., and Calonico, D.: Ultrastable laser interferometry for earthquake detection with terrestrial and submarine cables, Science, 361, 486–490, https://doi.org/10.1126/science.aat4458, 2018.

Parker, L. M., Thurber, C. H., Zeng, X., Li, P., Lord, N. E., Fratta, D., Wang, H. F., Robertson, M. C., Thomas, A. M., Karplus, M. S., Nayak,
400   A., and Feigl, K. L.: Active source seismic tomography at the Brady geothermal field, Nevada, with dense nodal , Seismological Research Letters, 89, 1629–1640, https://doi.org/10.1785/0220180085, 2018.

Piana Agostinetti, N. and Martini, F.: Sedimentary basins investigation using teleseismic P-wave time delays, Geophysical Prospecting, 67, 1676–1685, https://doi.org/10.1111/1365-2478.12747, 2019.

Shevenell, L. and De Rocher, T.: Evaluation of Chemical Geothermometers for Calculating Reservoir Temperatures at Nevada Geothermal
405   Power Plants,, in: Geothermal Resources Council Transactions, vol. 29, p. 303–308, 2005.

Sladen, A., Rivet, D., Ampuero, J. P., Barros, L. D., Hello, Y., Calbris, G., and Lamare, P.: Distributed sensing of earthquakes and ocean-solid Earth interactions on seafloor telecom cables, Nat. Comm., 10, 5777, https://doi.org/10.1038/s41467-019-13793-z, 2019.

Sleeman, R. and van Eck, T.: Robust automatic P-phase picking: an on-line implementation in the analysis of broadband seismogram recordings, Physics of the Earth and Planetary Interiors, 113, 265–275, https://doi.org/https://doi.org/10.1016/S0031-9201(99)00007-2, 1999.

410   Tarantola, A.: Inverse Problem Theory and Methods for Model Parameter Estimation, SIAM, 2005.

Tilmann, F. J., Sadeghisorkhani, H., and Mauerberger, A.: Another look at the treatment of data uncertainty in Markov chain Monte Carlo inversion and other probabilistic methods, Geophysical Journal International, 222, 388–405, https://doi.org/10.1093/gji/ggaa168, 2020.

van den Ende, M. P. A. and Ampuero, J.-P.: Evaluating Seismic Beamforming Capabilities of Distributed Acoustic Sensing Arrays, Solid Earth Discussions, 2020, 1–24, https://doi.org/10.5194/se-2020-157, 2020.

415   VanDecar, J. C. and Crosson, R. S.: Determination of teleseismic relative phase arrival times using multi-channel cross-correlation and least squares, Bulletin of the Seismological Society of America, 80, 150, 1990.

Wang, H. F., Zeng, X., Miller, D. E., Fratta, D., Feigl, K. L., Thurber, C. H., and Mellors, R. J.: Ground motion response to an ML 4.3 earthquake using co-located distributed acoustic sensing and seismometer arrays, Geophysical Journal International, 213, 2020–2036, https://doi.org/10.1093/gji/ggy102, 2018.

420 Ward Neale, J., Harmon, N., and Srokosz, M.: Improving Microseismic P Wave Source Location With Multiple Seismic Arrays, Journal of Geophysical Research: Solid Earth, 123, 476–492, https://doi.org/https://doi.org/10.1002/2017JB015015, 2018.

Wessel, P. and Smith, W. H. F.: New, improved version of the Generic Mapping Tools released, EOS Trans. AGU, 79, 579, 1998.

You, Y.: Harnessing telecoms cables for science, Nature, 466, 690–691, 2010.

Yu, C., Zhan, Z., Lindsey, N. J., Ajo-Franklin, J. B., and Robertson, M.: The Potential of DAS in Teleseismic Studies: Insights From the
425 Goldstone Experiment, Geophysical Research Letters, 46, 1320–1328, https://doi.org/https://doi.org/10.1029/2018GL081195, 2019.

Zeng, X., Lancelle, C., Thurber, C., Fratta, D., Wang, H., Chalari, A., and Clarke, A.: Properties of Noise Cross-Correlation Functions Obtained from a Distributed Acoustic Sensing Array at Garner Valley, California, Bulletin of the Seismological Society of America(, 107, http://dx.doi.org/10.1785/0120160168, 2017.
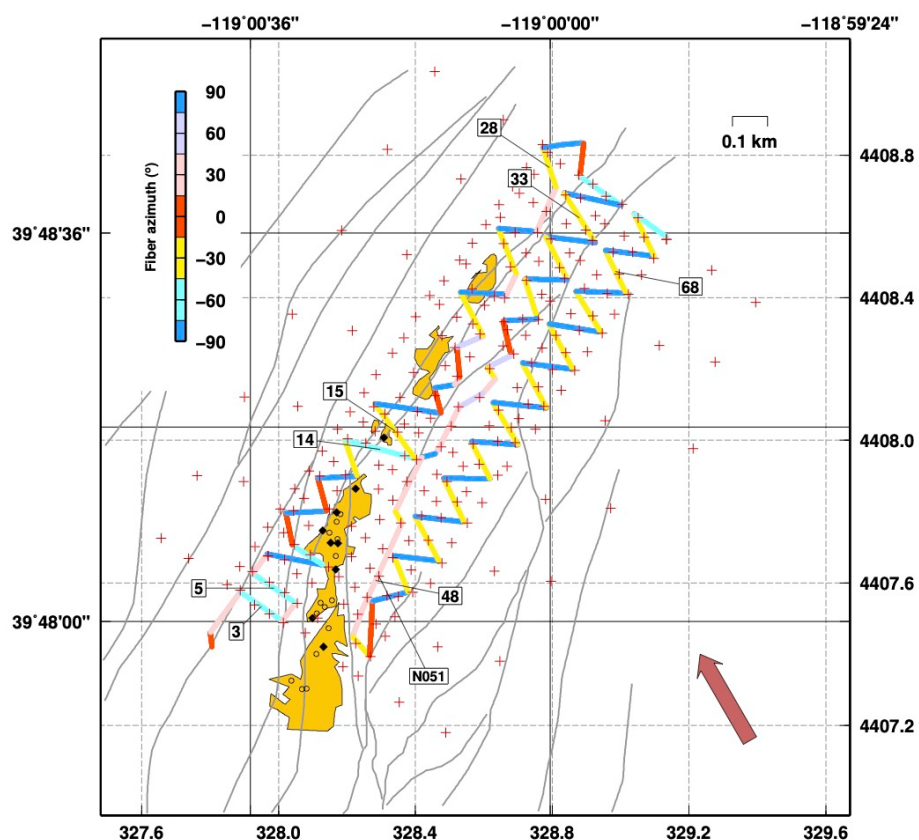
Figure 1. Porotomo experiment map: Fibre cable used for DAS (coloured line, colours indicate average azimuth of the segments), Numbers indicate segments described in the text; Nodal stations; faults (grey lines), warm ground (yellow areas); fumaroles (black diamonds) and mud-volcanoes (open diamonds). A red arrow indicates the direction of incoming P-Wave for the Mw 4.3 Hawthorne earthquake.
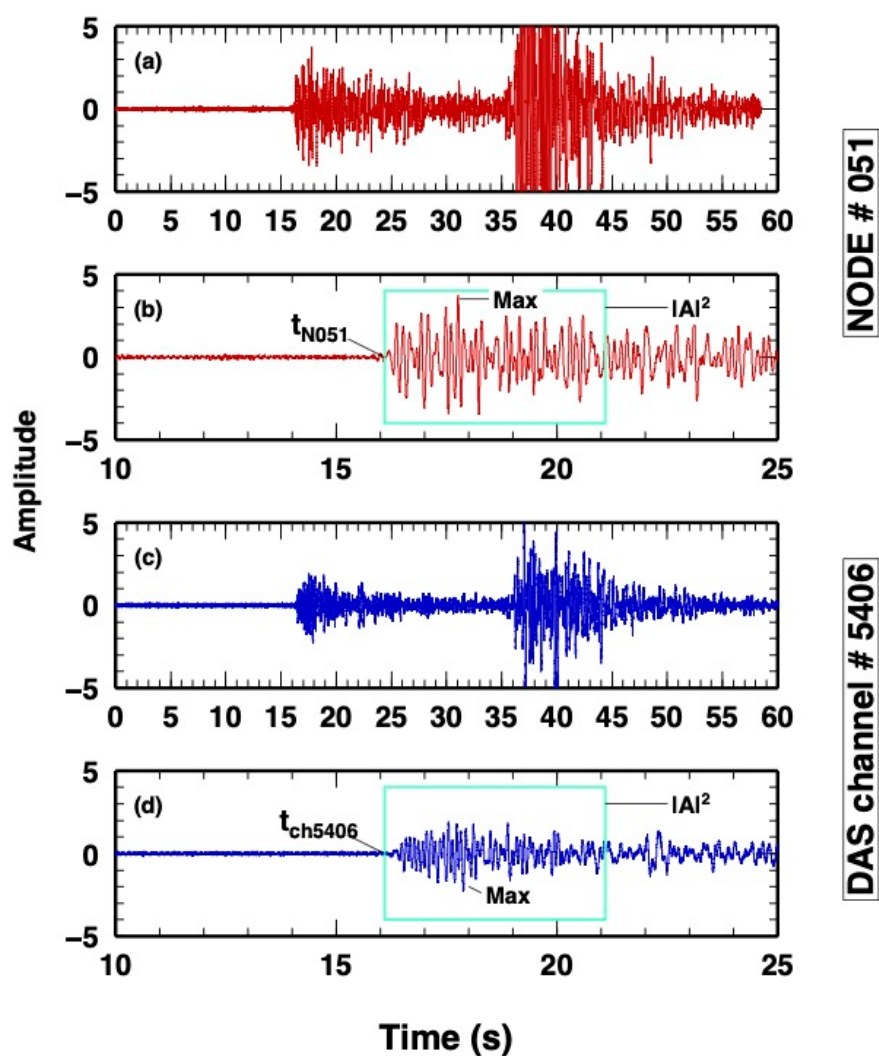
Figure 2. Waveforms generated from the Mw4.3 Hawthorne earthquake, with a zoom on P-wave with the quantities analysed in the study: P-wave arrival time, MAX amp, Energy in the P-window (for computing SNR). Node 51: (a) and (b); Closest DAS channel to Node 51 (channel number 5406): (c) and (d)
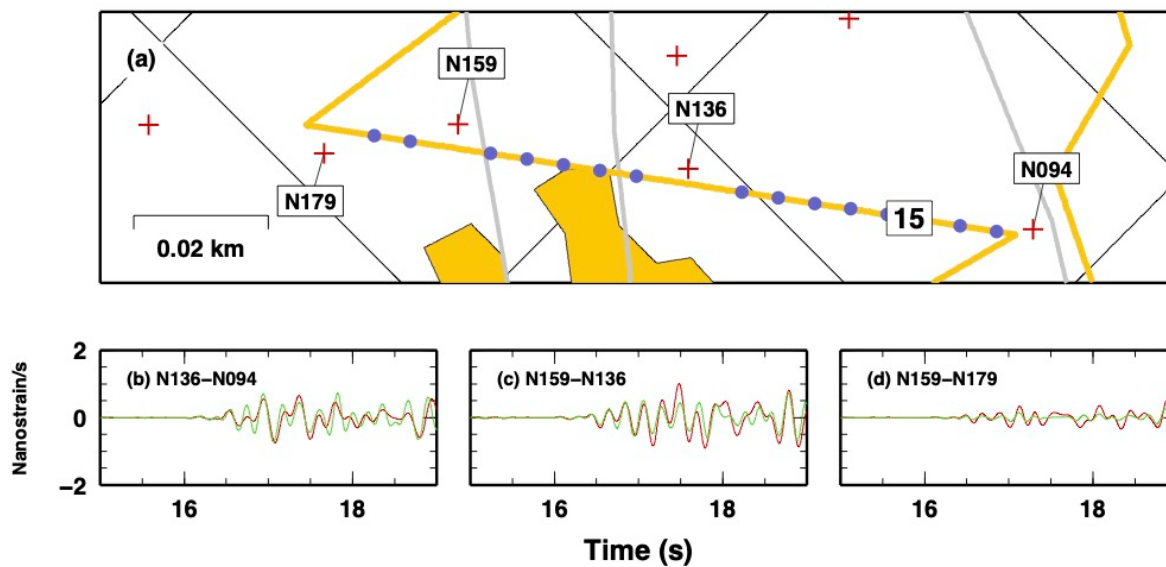
Figure 3. Comparison of DAS and NODAL recordings, following Wang et al. (2018) Equation 5. (a) Map of DAS segment 15 and co-located Nodes. P-wave arrival in the three sub-segments as local derivative of strain, between: (b) Node 94 and Node 136; (c) Node 136 and Node 159; (d) Node 159 and Node 179.
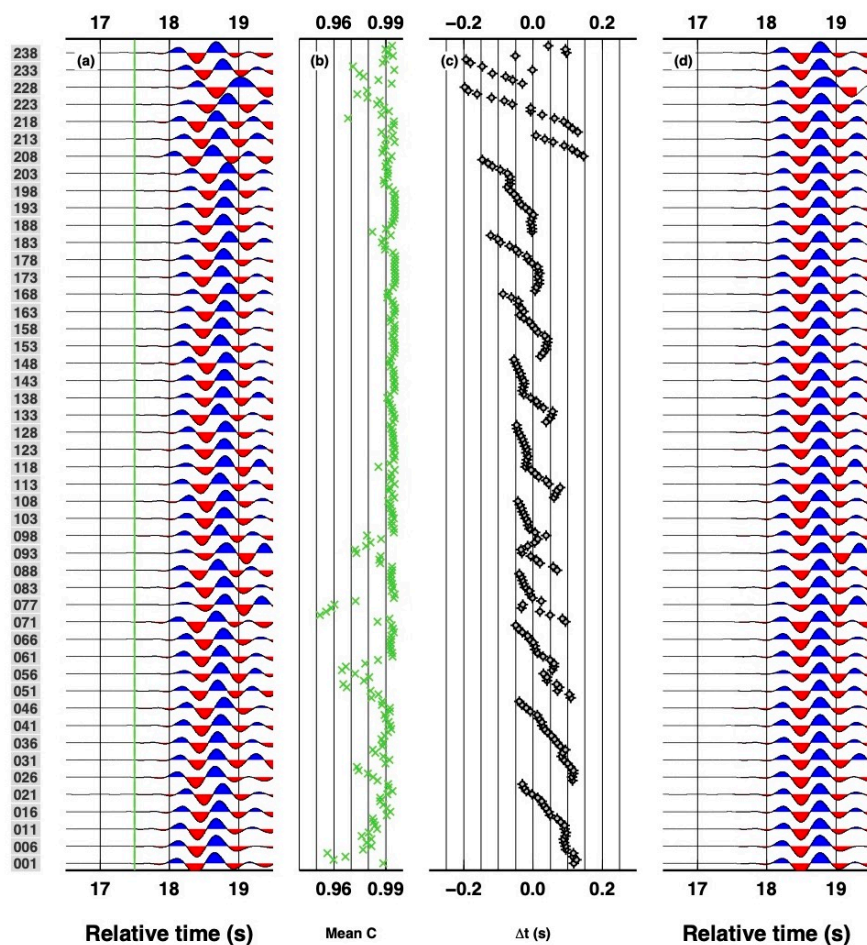
Figure 4. Example of analysis for computing P-wave time-delays using VanDecar and Crosson (1990)'s approach applied to Vertical recordings of Nodal seismometers. (a) Original waveforms filtered between 0.5-2 Hz showing P-wave arrivals. (b) Average cross-correlation value, for each station cross-correlated to all others. (c) Relative P-wave time-delays. (d) Aligned P-wave arrival using time-delays in (c). Stations are ordered with station names. Only one every five stations is shown in panels (a) and (d) for clarity.
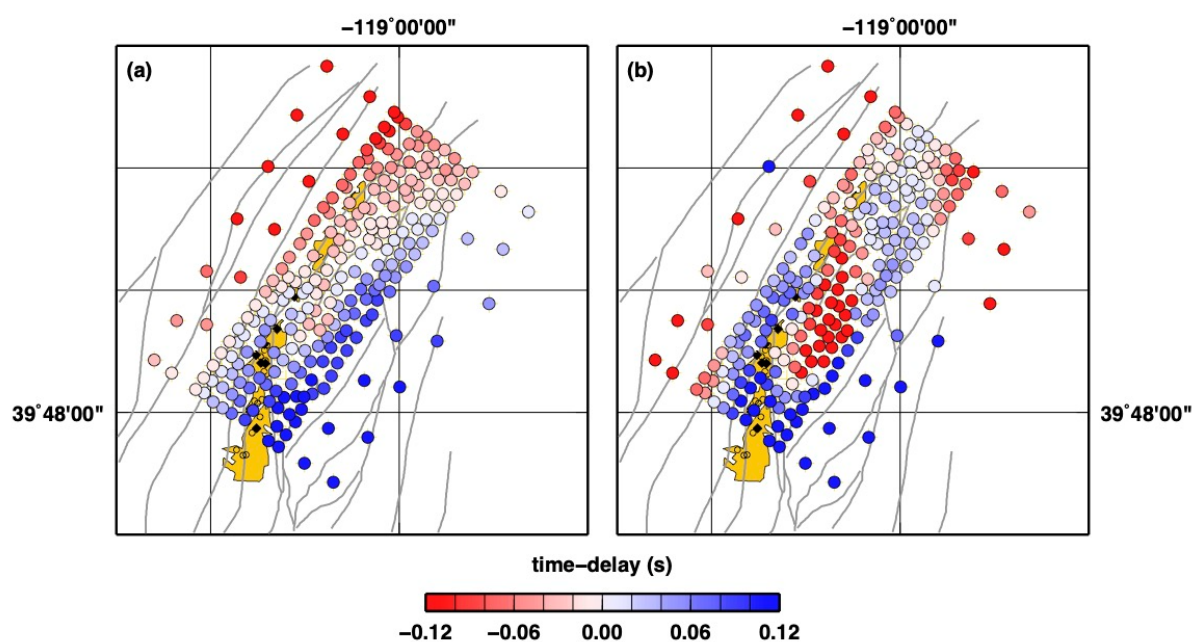
Figure 5. Maps of P-wave time-delay from correlation of recordings by Nodal stations. Waveforms have been filtered to 0.5-2.0Hz: (a) Vertical components; (b) North components.
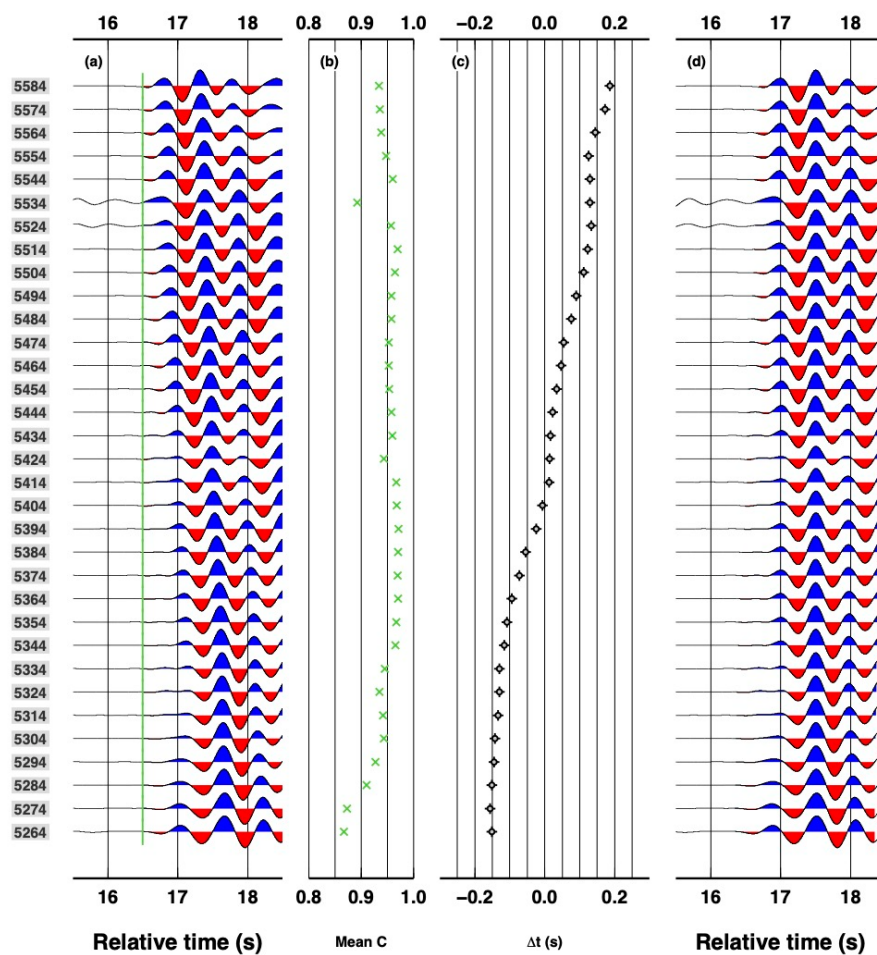
Figure 6. Example of analysis for computing P-wave time-delays using VanDecar and Crosson (1990)'s approach applied to DAS channels along segment 48. Same panels as in Figure 4.
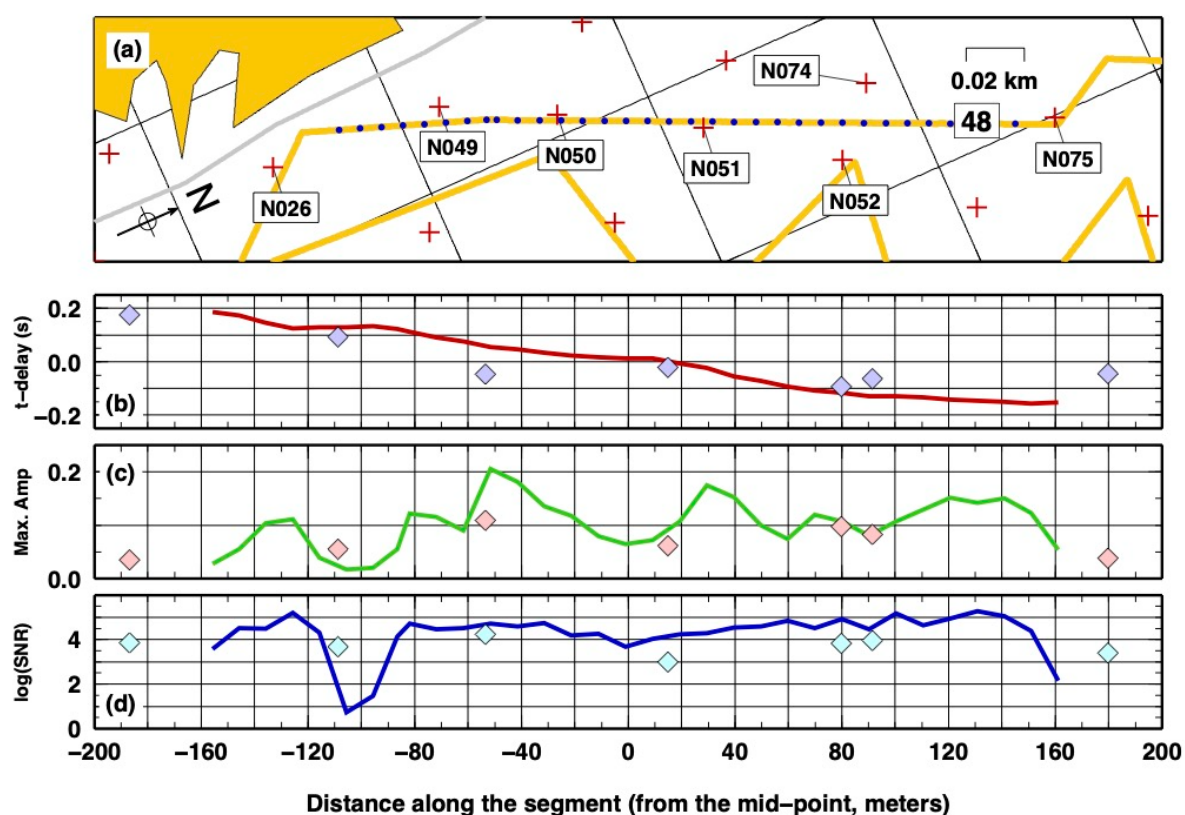
Figure 7. Measurements along the single DAS segment 48 (coloured lines), compared to measurements obtained using rotated horizontal recordings of co-located Nodal stations (grey diamonds). (a) Map of the DAS segments. (b) P-wave time-delays, (c) maximum amplitude and (d) log(SNR) as a function of the distance along the cable segment.
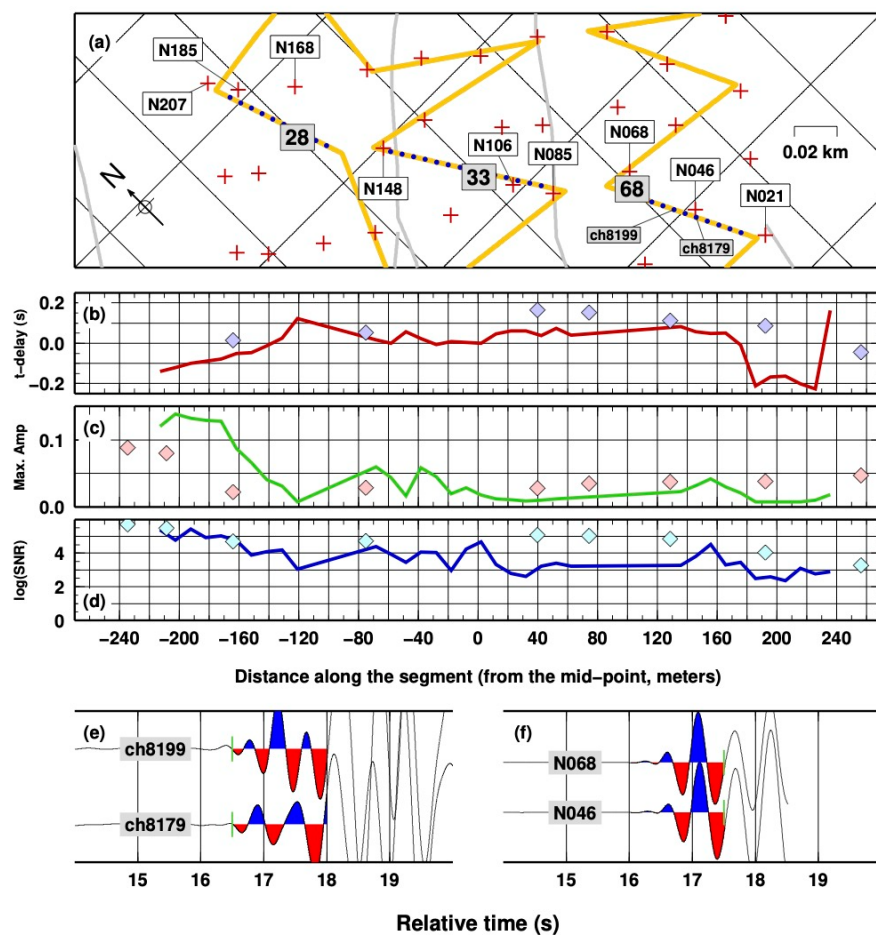
Figure 8. Same as Figure 7, but for three consecutive (almost parallel) DAS segments: 68, 33 and 28. (e-f) Examples of waveforms recorded at DAS (e) and nodes (f).
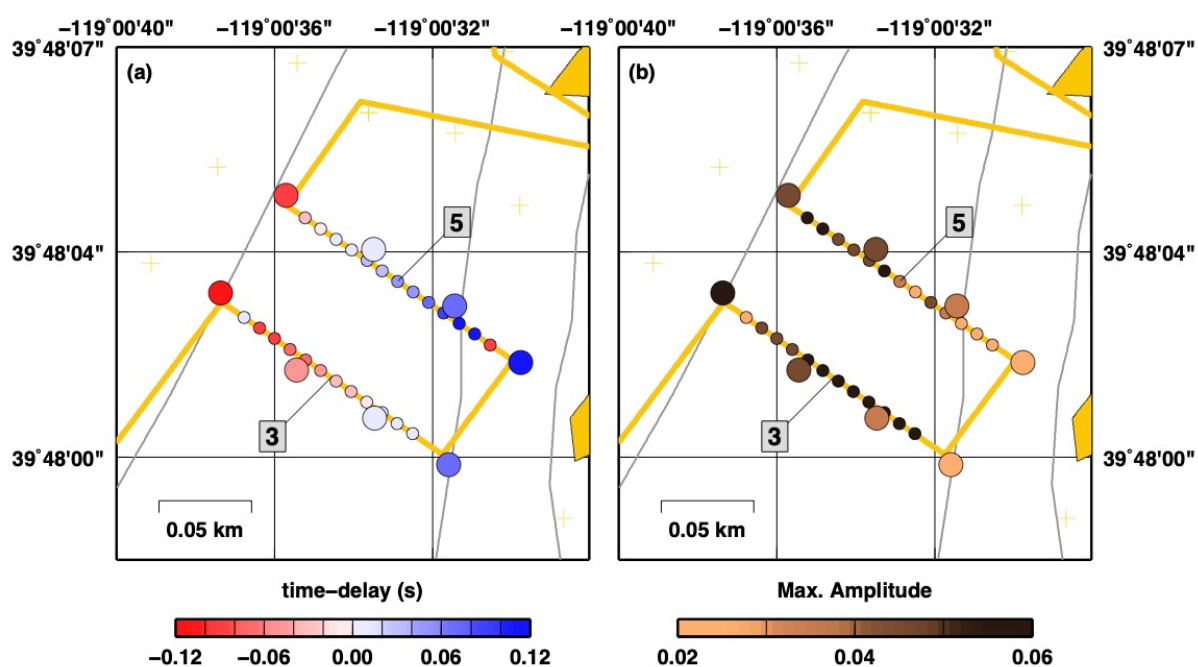
Figure 9. Map of: (a) P-wave time-delays and (b) maximum amplitude for two parallel DAS segments: 3 and 5 (small coloured circles). Results for co-located Nodal stations are also presented (large coloured circles).
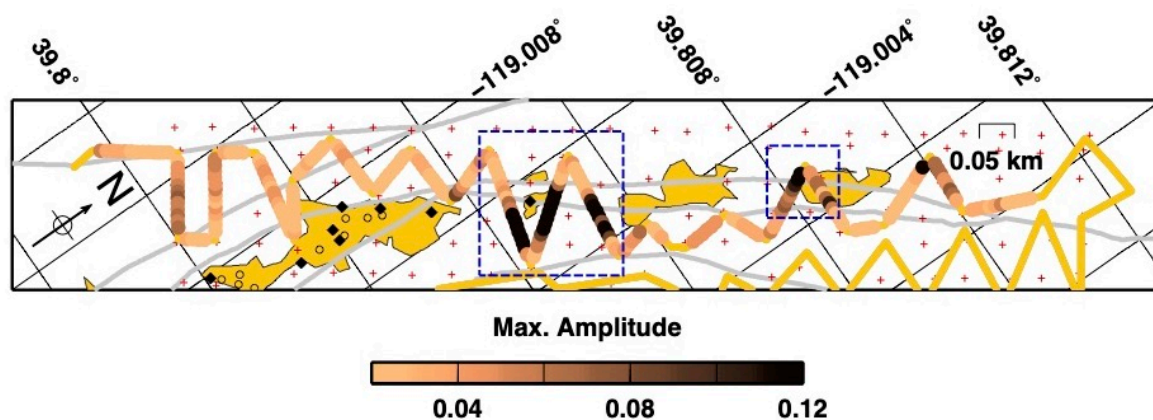
Figure 10. Amplitude analysis for all DAS segments along the northwestern side of the Porotomo experiment (segments from from 1 to 30). The dashed box indicate the area of maximum amplitude, which correspond to the fibre cable crossing the warm-ground and the area of the fumaroles/mud-volcanoes.
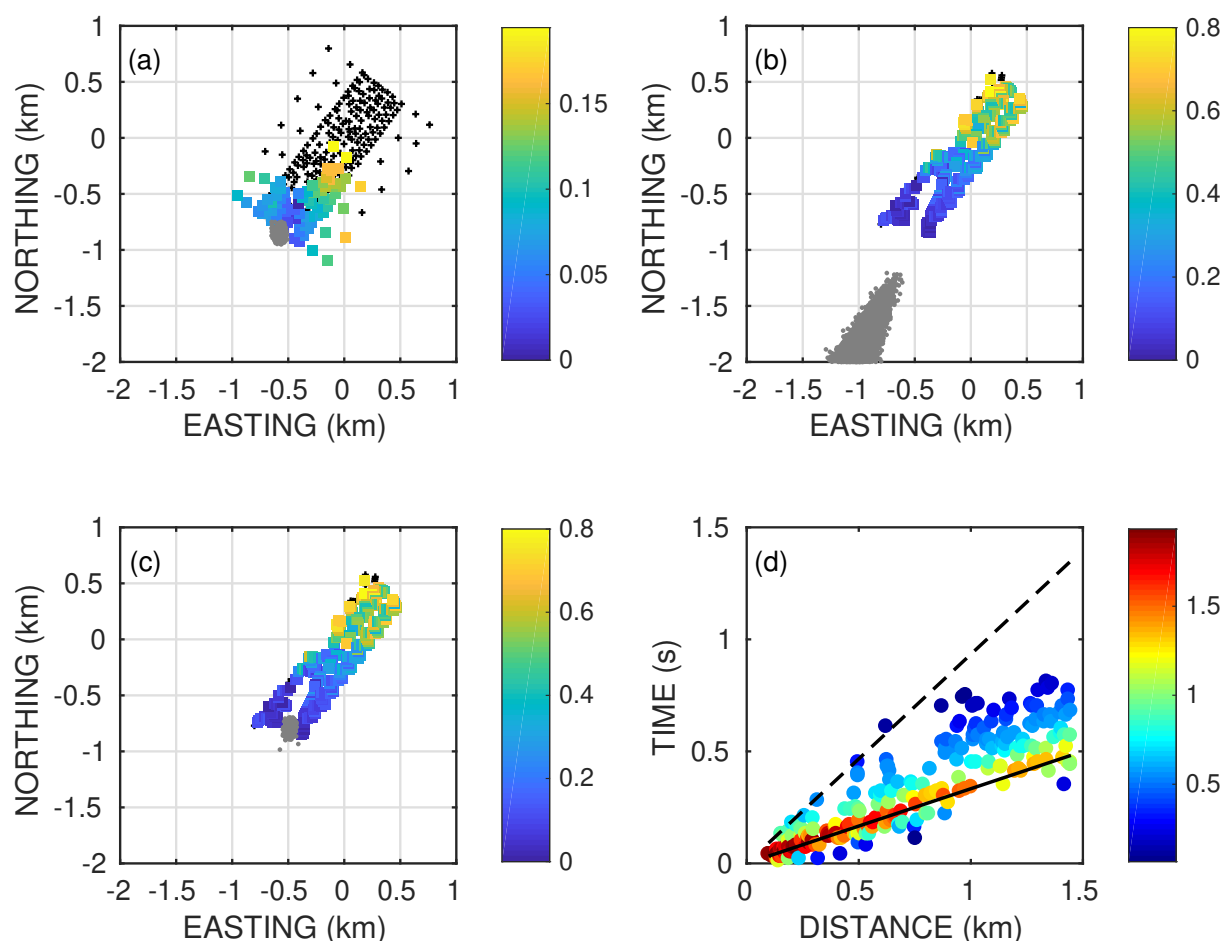
Figure 11. (a) Samples of the likelihood function of source location (gray dots) resulting from travel-time inversion of the local earthquake recorded at the nodal array (crosses). Colors indicate the timing of manually-picked P-wave arrivals, according to the color scale at the right. (b) The same as in (a), but for the automatic picking obtained at the 274-element virtual DAS array. Most samples of the likelihood function for source location are clipped at the grid boundary. (c) The same as in (b), but inverting the differential times at the DAS array. (d) Arrival times derived from automatic pickings at the DAS array as a function of epicentral distance. Colors refer to the posterior phase weights based on the contribution of the observation to the maximum likelihood EDT solution, according to the color scale at the right. The continuous and dashed lines indicate the moveout of P- and S-waves, respectively, in the homogeneous velocity structure used for calculating the theoretical travel times.
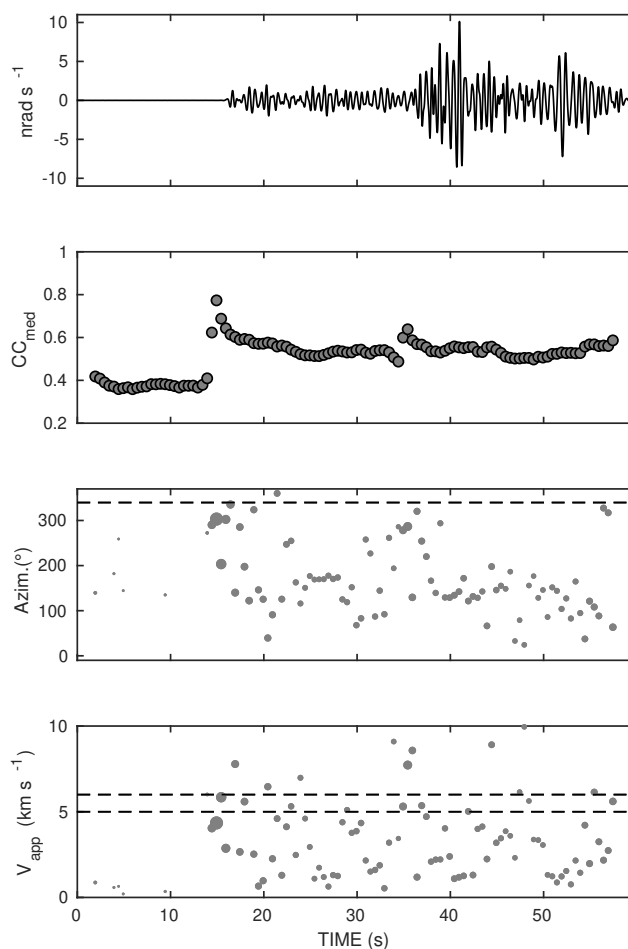
Figure 12. Results from fitting a plane wave to DAS differential times. (a) Recording of the Hawthorne earthquake from a sample DAS stacked channel. Data are band-pass filtered over the 0.5-2Hz frequency band. (b) Median of C_{ij}^{max} from all independent channels of the DAS stacked channels. (c) Propagation azimuth; the size of the points is proportional to the average correlation of the channels used for the inversion. The dashed line indicates the theoretical propagation azimuth ($337°$ clockwise from the N direction). (d) Apparent velocity, derived from the inverse of the modulus of the horizontal slowness vector. The dashed lines mark the velocity range obtained by VdEA2020 from analysis of the nodal array data.